



3D structured illumination microscope using a spinning disk [Invited]

YOUCHANG ZHANG,¹ PARISA ASGHARI,² DAVID R. L. SCRIVEN,² 
EDWIN D. W. MOORE,^{2,3} AND KENG C. CHOU^{1,4} 

¹*Department of Chemistry, Life Sciences Institute, University of British Columbia, Vancouver, BC V6T 1Z1, Canada*

²*Department of Cellular and Physiological Sciences, Life Sciences Institute, University of British Columbia, Vancouver, BC V6T 1Z3, Canada*

³*edwin.moore@ubc.ca*

⁴*kcchou@chem.ubc.ca*

Abstract: Three-dimensional (3D) structured illumination microscopy (SIM) improves spatial resolution by a factor of two in both lateral and axial directions. However, the adoption of 3D SIM is limited by low imaging speed, susceptibility to out-of-focus light, and likelihood of reconstruction errors. Here we present a novel approach for 3D SIM using a spinning disk. The disk generates a 3D lattice illumination pattern on the sample and optically reconstructs super-resolved images in real time. This technique achieves a 2-times resolution improvement with a speed up to 100 frames per second while physically rejecting 90% of the background signal.

© 2023 Optica Publishing Group under the terms of the [Optica Open Access Publishing Agreement](#)

1. Introduction

The spatial resolution in conventional light microscopy is limited to approximately 250 nm laterally and 750 nm axially because of diffraction. This limitation hinders direct observation of subcellular structures, impeding the study of biological phenomena. In recent decades, various efforts have been made to enhance the resolution beyond the diffraction limit [1–5]. Among these methods, structured illumination microscopy (SIM) [1,3] has emerged as the most suitable method for high-speed super-resolution imaging, because it offers a relatively high imaging speed and low phototoxicity in comparison to other super-resolution imaging techniques.

Despite three-dimensional (3D) SIM's superior resolution in both lateral and axial directions [6], it has several limitations. While conventional two-dimensional (2D) SIM requires 9 diffraction-limited images to digitally reconstruct one super-resolved image, 3D SIM requires at least 15 images [6], which limits the imaging speed and makes it sensitive to sample motion. Additionally, conventional 3D SIM uses wild-field illumination patterns created by 3-beam interference. It has significant out-of-focus signals, making it difficult to extract the high-frequency components required for improving the resolution. It is particularly problematic to image thick samples when the out-of-focus signals overwhelm the in-focus signals [6,7]. Furthermore, 3D SIM images are prone to reconstruction artifacts because it has less tolerance for the distortion of the illumination patterns. However, distortion is often inevitable because of aberration and refractive index mismatch.

In this paper, we present a novel approach for 3D SIM that utilizes a spinning disk to overcome these limitations. The disk, fabricated by photolithography, creates a 3D lattice illumination pattern, and optically reconstructs the super-resolved images in real-time. It substantially increases the imaging speed up to 100 Hz, physically rejects 90% of background signals, and circumvents the complexities associated with digital reconstruction. Our approach is straightforward and can be incorporated into most existing epi-fluorescence microscopes. The performance of the

spinning-disk 3D SIM is validated by imaging fluorescent beads and rat cardiac myocytes with a thickness of $\sim 12 \mu\text{m}$.

2. Theory

In conventional fluorescence microscopy, the fluorescent emission $e(\mathbf{r})$ is blurred by the point spread function (PSF) $h(\mathbf{r})$ and produces the final image $i(\mathbf{r})$. The bandwidth of the final image in the spatial frequency domain is limited by the optical transfer function (OTF) $H(\mathbf{k})$

$$I(\mathbf{k}) = E(\mathbf{k}) \times H(\mathbf{k}) \quad (1)$$

The capital letters indicate the Fourier transform of their corresponding functions in the real space. SIM optically modulates the sample frequencies by exciting the sample fluorophore distribution $s(\mathbf{r})$ with a patterned illumination $j(\mathbf{r})$

$$I(\mathbf{k}) = [S(\mathbf{k}) \otimes J(\mathbf{k})] \times H(\mathbf{k}) \quad (2)$$

where $S(\mathbf{k}) \otimes J(\mathbf{k}) = E(\mathbf{k})$, and \otimes indicates convolution. $J(\mathbf{k})$ downshifts the sample frequencies in $S(\mathbf{k})$ that used to be beyond the cut-off frequency $|k_{\text{cut-off}}|$ of $H(\mathbf{k})$ into the support of $H(\mathbf{k})$. In the post-processing, the frequency demodulation is accomplished by digitally identifying these frequency components and upshifting them to their original positions.

Previous work by Hayashi et al. shows that SIM images can be optically demodulated by passing the patterned emission through the same spinning disk that creates the illumination pattern $j(\mathbf{r})$ [8]. However, the resolution improvement of Hayashi's work is limited to 2D. Here we show that 3D resolution enhancement can be obtained. To simplify the mathematical derivation, the magnification of the imaging system is neglected.

For fluorophore excitation, the disk, which is denoted by $disk(\mathbf{r})$, creates its diffraction-limited projection on the sample as an illumination pattern $j(\mathbf{r})$. Therefore, in the frequency space, $J(\mathbf{k})$ is the collection of the low frequency components in $Disk(\mathbf{k})$

$$Disk(\mathbf{k}) = J(\mathbf{k}) + Disk_{\text{high}}(\mathbf{k}) \quad (3)$$

where $Disk_{\text{high}}(\mathbf{k})$ represents the high frequency components in $Disk(\mathbf{k})$ that is beyond $|k_{\text{cut-off}}|$. \mathbf{r} and \mathbf{k} are 3D vectors. Equation (3) applies only when the disk is an amplitude grating, not a phase grating.

The fluorescent emission $e(\mathbf{r})$ is then collected by the objective lens and transmits through the disk before reaching the camera. Because the disk is an amplitude grating, the disk function $disk(\mathbf{r})$ remains the same for both the coherent illumination and the incoherent fluorescence emission. When the disk is stationary, the Fourier transform of the detected image $i_s(\mathbf{r})$ follows

$$\begin{aligned} I_s(\mathbf{k}) &= \{[S(\mathbf{k}) \otimes J(\mathbf{k})] \times H(\mathbf{k})\} \otimes Disk(\mathbf{k}) \\ &= \{[S(\mathbf{k}) \otimes J(\mathbf{k})] \times H(\mathbf{k})\} \otimes [J(\mathbf{k}) + Disk_{\text{high}}(\mathbf{k})] \end{aligned} \quad (4)$$

When the disk spins, the final image detected by the camera is a time average of the stationary images at different positions \mathbf{r} . Assuming that the disk conducts a spatially uniform scan across the specimen, the Fourier transform of the final image $i_f(\mathbf{r})$ detected by the camera is the integral of $I_s(\mathbf{k})$ over \mathbf{r} :

$$I_f(\mathbf{k}) = \int I_s(\mathbf{k}) d\mathbf{r} \quad (5)$$

The translational property of the Fourier transform asserts that: for any give shift \mathbf{r}_0 , $T(\mathbf{k}) = \exp(i2\pi\mathbf{r}_0 \cdot \mathbf{k})G(\mathbf{k})$ if $t(\mathbf{r}) = g(\mathbf{r} - \mathbf{r}_0)$. Therefore, Eq. (5) can be expanded to

$$\begin{aligned} I_f(\mathbf{k}) &= \int I_s(\mathbf{k}) d\mathbf{r} \\ &= \int \{[S(\mathbf{k}) \otimes (\exp(i2\pi\mathbf{r} \cdot \mathbf{k})J(\mathbf{k}))] \times H(\mathbf{k})\} \otimes [\exp(i2\pi\mathbf{r} \cdot \mathbf{k})J(\mathbf{k})] d\mathbf{r} + \\ &\quad \int \{[S(\mathbf{k}) \otimes (\exp(i2\pi\mathbf{r} \cdot \mathbf{k})J(\mathbf{k}))] \times H(\mathbf{k})\} \otimes [\exp(i2\pi\mathbf{r} \cdot \mathbf{k})Disk_{high}(\mathbf{k})] d\mathbf{r} \end{aligned} \quad (6)$$

Because the integral of the complex exponential function is zero ($\int \exp(i\mathbf{r}) d\mathbf{r} = 0$), the integral of $\int \exp(i\mathbf{r} \cdot \mathbf{k})g(\mathbf{k})d\mathbf{r}$ always equals to zero. The first integral in Eq. (6) produces non-zero results only when the two complex exponential terms inside the equation cancel with each other. To find the condition for the non-zero requirement, we need an explicit expression of $J(\mathbf{k})$. Because the illumination pattern $j(\mathbf{r})$ is a real function, its Fourier transform $J(\mathbf{k})$ is an even function. Therefore, for a given value of \mathbf{k} , $J(\mathbf{k})$ and $J(-\mathbf{k})$ have equal amplitudes and inverse phases. Consequently, $J(\mathbf{k})$ can be described as

$$\begin{aligned} J(\mathbf{k}) &= \sum_p a_p \exp(-i2\pi\mathbf{k}_p \cdot \mathbf{r}_0) \delta(\mathbf{k} - \mathbf{k}_p) \\ &= a_0 \delta(\mathbf{k}) + \\ &= a_1 \exp(-i2\pi\mathbf{k}_1 \cdot \mathbf{r}_0) \delta(\mathbf{k} - \mathbf{k}_1) + a_{-1} \exp(-i2\pi\mathbf{k}_{-1} \cdot \mathbf{r}_0) \delta(\mathbf{k} - \mathbf{k}_{-1}) + \\ &= a_2 \exp(-i2\pi\mathbf{k}_2 \cdot \mathbf{r}_0) \delta(\mathbf{k} - \mathbf{k}_2) + a_{-2} \exp(-i2\pi\mathbf{k}_{-2} \cdot \mathbf{r}_0) \delta(\mathbf{k} - \mathbf{k}_{-2}) + \dots \end{aligned} \quad (7)$$

where \mathbf{r}_0 is the initial position of the disk before spinning, p are integers, $a_p = a_{-p}$, $-\mathbf{k}_p = \mathbf{k}_{-p}$. a_p are constant coefficients determined by the size of the openings on the disk. \mathbf{k}_p , located in the 3D frequency space, are determined by the period of the openings on the disk [9]. The delta functions in Eq. (7) shifts the sample frequencies $S(\mathbf{k})$ by convolution, while the complex exponential terms modulate the phase. The only condition for the first integral in Eq. (6) to be non-zero is that the amount of the phase change shifted by the first $\exp(i2\pi(\mathbf{r} - \mathbf{r}_0) \cdot \mathbf{k})$ happens to be cancelled by the second exponential term, i.e., $\exp(i2\pi(\mathbf{r} - \mathbf{r}_0) \cdot \mathbf{k}_p) \times \exp(i2\pi(\mathbf{r} - \mathbf{r}_0) \cdot \mathbf{k}_{-p}) = 0$. Under this condition, the frequency shifts in $S(\mathbf{k})$ introduced by the first $J(\mathbf{k})$ in the first integral in Eq. (6) is recovered by their opposite delta functions in the second $J(\mathbf{k})$ in an analog way: $[S(\mathbf{k}) \otimes \delta(\mathbf{k} - \mathbf{k}_p)] \otimes \delta(\mathbf{k} - \mathbf{k}_{-p}) = S(\mathbf{k})$. Therefore, the first integral in Eq. (6) is simplified as

$$S(\mathbf{k}) \sum_p a_p^2 H(\mathbf{k} - \mathbf{k}_p) \quad (8)$$

To fulfill the same non-zero requirement, complex exponential terms in the second integral of Eq. (6) also need to cancel. However, the frequency components in $Disk_{high}(\mathbf{k})$ have amplitudes higher than $|\mathbf{k}_{cut-off}|$, while the amplitudes of frequency components in $J(\mathbf{k})$ are smaller than $|\mathbf{k}_{cut-off}|$. Consequently, there is no \mathbf{k}_{-p} in the second exponential term to cancel the phase change induced by the \mathbf{k}_p in the first exponential term. Therefore, the second integral in Eq. (6) is zero, and Eq. (6) produces

$$I_f(\mathbf{k}) = \int I_s(\mathbf{k}) d\mathbf{r} = S(\mathbf{k}) \sum_p a_p^2 H(\mathbf{k} - \mathbf{k}_p) = S(\mathbf{k}) H_{sim}(\mathbf{k}) \quad (9)$$

where $H_{sim}(\mathbf{k})$ is the optical transfer function of the spinning-disk structured illumination microscope.

Compared to the wide-field OTF $H(\mathbf{k})$, the support of the OTF $H_{sim}(\mathbf{k})$ is expanded by the frequency components \mathbf{k}_p in the illumination pattern $J(\mathbf{k})$. When $j(\mathbf{r})$ has intensity variation in

both lateral and axial directions, its frequency components \mathbf{k}_p occupy regions in the 3D frequency space, thus it enhances spatial resolution in 3D. Additionally, when components of \mathbf{k}_p shift the $H(\mathbf{k})$ with a lateral distance less than $|\mathbf{k}_{cut-off}|$, the shifted OTF fills the missing-cone region axially, and enables optical sectioning capability [6]. In the formation of the final image, \mathbf{k}_p spin around the \mathbf{k}_z axis in the frequency domain as the disk spins. Therefore, deriving an analytical expression for the effective OTF $H_{sim}(\mathbf{k})$ is difficult. In this study, the OTF of the spinning-disk 3D SIM is simulated numerically in section 4.2.

In the above derivation, prior knowledge of the disk's pattern is not required, meaning that any amplitude grating can be employed, irrespective of its pattern. However, to achieve optimal resolution enhancement and optical sectioning capability, the disk is chosen to have a period d close to $2/|\mathbf{k}_{cut-off}|$.

3. Method

3.1. Optical setup

Figure 1 shows the diagram of the optical setup. A 488 nm laser (Coherent, Sapphire 488) is used for excitation. The laser beam (blue) is circularly polarized by a quarter wave plate (Thorlabs, WPQ10M-488) to achieve a higher illumination contrast [10]. After being expanded by a convex lens ($f = 50$ mm) and a relay lens RL1 (Thorlabs, TTL200, $f = 200$ mm), the collimated laser beam passes through the spinning disk. The disk employed in this study is an amplitude grating. The period of the grating is around 84 μm , allowing the 0th-order and four 1st-order diffraction beams to be focused by the tube lens TL (Thorlabs, TL300-A, $f = 300$ mm) and enter the back pupil of the objective lens (Olympus, UPLSAPO100XS, NA = 1.35). The image of the incident laser beams at the back pupil is shown in Figure S1. The objective lens illuminates the sample with the interference pattern produced by these 5 laser beams. In the detection pathway, the emission (green in Fig. 1) is collected by the objective lens and focused on the disk by the TL. This system has a magnification of 167 times. The disk optically reconstructs the super-resolved images when spinning. The image on the spinning disk is then relayed by the lens pair RL1 and RL2 (Thorlabs, TTL200, $f = 200$ mm) to the camera (Hamamatsu, C13440-22CU) after passing through a dichroic mirror (Omega, 555DRLP) and a filter (Semrock, FF03-525/50), with a field of view of $\sim 80 \mu\text{m} \times 80 \mu\text{m}$. The camera has a frame rate up to 100 Hz. The disk is mounted on a brushless DC motor, which rotates up to 7200 rpm. As one super-resolved image can be reconstructed each time the disk completes one rotation, the imaging speed of this system is limited by the speed of the camera, i.e., 100 Hz.

3.2. Design and fabrication of the spinning disk

The design of the disk is demonstrated in Fig. 2(a). An aluminum layer (thickness ~ 120 nm) with an array of pinholes is deposited on an optically-flat fused silica substrate (University Wafer, JGS2) by photolithography. The pinholes have a diameter (w) of 28 μm and a period (d) of 84 μm . The pinholes on the disk are partitioned into 8 sectors with offsets. The pinholes within each sector are displaced collectively along their central radial directions. The offsets are as follows: 19.5 μm , 216.1 μm , 27.2 μm , 51.4 μm , 4.8 μm , 26.5 μm , 221.0 μm , and 58.8 μm . The offsets across various sectors ensure that the sample is uniformly scanned as the disk spins. Without these offsets, the pinholes are not uniformly distributed along the radial direction, resulting in fringes in the images. To achieve an uniform scan, the conventional solution is to rearrange the pinholes along Archimedean spirals, known as the Nipkow disk [11]. However, this approach compromises resolution improvement in SIM. Compared to an unpartitioned pinhole array, our simulation shows that the 8-sector design with the radial offsets increases the scanning uniformity from 72.7% to 94.4% (Fig. 2(c)). Moreover, this design exhibits a high degree of tolerance for the disk off-centering. Off-centering occurs when the disk's center does not precisely align with

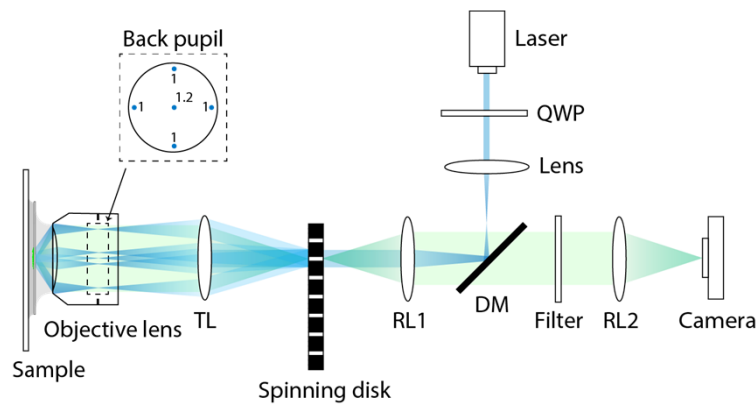


Fig. 1. Diagram of the optical setup. TL: tube lens. RL: relay lens. DM: dichroic mirror. QWP: quarter wave plate. Blue: excitation laser. Green: fluorophore emission. Inset: the excitation laser beam is diffracted to 5 beams at the objective lens back pupil. The numbers represent the relative intensities of these 5 beams.

the motor's spin axis. This design ensures that the scanning uniformity remains approximately 94.4% in the presence of the misalignment.

The disk opening ratio (w/d) is chosen to be $28\mu\text{m}/84\mu\text{m} = 33\%$. An image of the fabricated disk is shown in Fig. 2(b). At this ratio, 90% of the disk is covered by the opaque aluminum layer. Consequently, the disk physically rejects 90% of the out-of-focus signals, achieving a better contrast compared to the conventional 3D SIM. A smaller opening ratio can further reduce the out-of-focus signals but will decrease the signal-to-noise ratio SNR. 33% is chosen to be a good balance between background rejection and signal-to-noise ratio [8].

3.3. Preparation of the rat cardiac myocytes

Ventricular myocytes were isolated from the hearts of adult-male Wistar rats weighing between 200 and 250 g. Techniques for acquiring myocytes and for fixation and permeabilization have been published [12]. To identify the position of the type II ryanodine receptor (RyR2) in the fixed myocytes we used a mouse monoclonal antibody C3-33 (R-128 Sigma-Aldrich) and a goat anti-mouse secondary antibody conjugated to Alexa 488 (Invitrogen, Burlington, Canada). The secondary antibody was affinity purified and highly cross-adsorbed to minimize cross-reaction. Briefly, cells were fixed with 2% paraformaldehyde for 10 min, then quenched in 100 mM glycine and washed with PBS (3×10 min). They were then permeabilized with 0.1% Triton for 10 min, and washed with PBS (3×10 min). Before the application of the primary antibody, the cells were incubated for 30 minutes at room temperature (RT) with Image-IT FX Signal Enhancer (I36933; Life Technologies) to neutralize the surface charge, washed briefly in PBS and then incubated for 1 hour at RT in BlockAid blocking solution (B10710; Life Technologies). The primary antibody was diluted in BlockAid before being applied to the cells (overnight at 4°C). Cells were then washed in PBS (3×10 min) and incubated at RT for 60 minutes with goat anti-mouse Alexa 488 and washed in PBS (3×10 min).

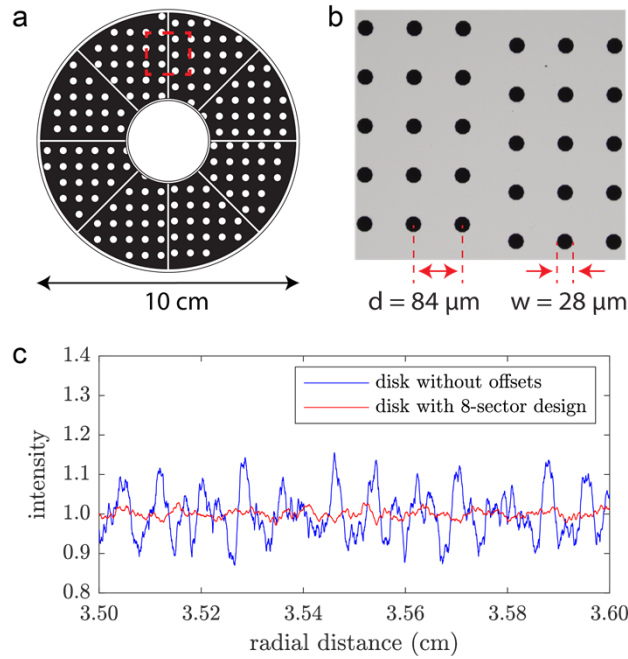


Fig. 2. Design of the spinning disk. (a) The disk with a diameter of 10 cm contains a 2D pinhole array. The pinholes on the disk are partitioned into 8 sectors with offsets in the radial direction (not depicted to scale for illustration purposes). (b) Image of the fabricated disk. The image shows a boundary of two sectors indicated by the red dashed box in (a). The pinhole array has a period of $84 \mu\text{m}$ and a diameter of $28 \mu\text{m}$. (c) Comparison of the scanning uniformity between the pinhole array without offsets (blue) and one being partitioned to 8 sectors (red). The uniformity is defined by I_{\min}/I_{\max} . The 8-sector design increases the uniformity from 72.7% to 94.4%. For better visual effect, only the cross-section ranging from 3.50 cm to 3.60 cm along the radial direction is shown. The average intensities are normalized to 1.

4. Results

4.1. Simulation of the 3D structured illumination patterns

The disk generates a 3D lattice illumination on the sample through the interference of 5 laser beams. After passing through the disk, the excitation laser beam is diffracted into one 0th-order and four 1st-order beams that enter the back pupil of the objective lens (Fig. 1 inset). In the 3D spatial frequency domain, the 0th-order beam possesses a distinct axial frequency compared to the 1st-order beams, as in Fig. 3(a) [13]. Consequently, they produce structured illumination patterns in both lateral and axial directions. The Fourier transform of the illumination pattern is the autocorrelation of the 5 beams, which exhibits 17 delta functions in the frequency space (Fig. 3(b)). These delta functions shift the object spectrum to 17 different positions, allowing the frequencies that are beyond the diffraction limit of the conventional OTF to be captured. With a disk period d of $84 \mu\text{m}$ (Fig. 2(b)) and a magnification of 167 times, the 3D lattice illumination generated in the focal volume has a lateral period $l_{xy} = 500 \text{ nm}$ (Fig. 3(c)) and axial period $l_z = 1072 \text{ nm}$ (Fig. 3(d)). The lattice illumination patterns were simulated using vectorial diffraction theory [14,15]. With circular polarization, the lattice illumination achieves a contrast of $\sim 88\%$.

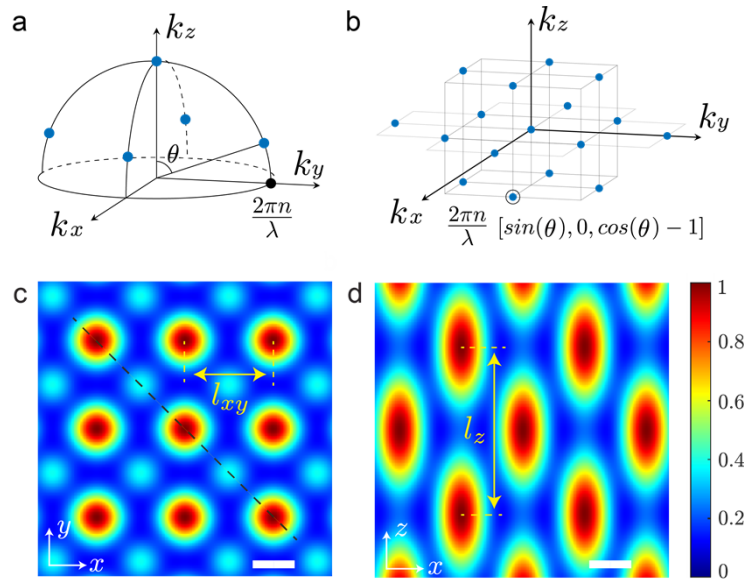


Fig. 3. Generation of the 3D lattice illumination. (a) Distribution of 5 coherent beams in the 3D frequency space. θ is the half-angle subtended by the four 1st-order beams with respect to the optical axis. For the disk with $d = 84 \mu\text{m}$, $\theta = 50^\circ$. n is the refraction index. λ is the excitation wavelength. (b) Autocorrelation of the 5 beams in (a), which is the Fourier transform of the illumination pattern. The resulting 17 delta functions expand the OTF both laterally and axially. (c) The cross-section of the illumination pattern in the $x - y$ plane. (d) The axial cross-section of the illumination pattern along the black dashed line in (c). The illumination resembles a 3D lattice with a lateral period $l_{xy} = 500 \text{ nm}$ and axial period $l_z = 1072 \text{ nm}$. The lattice has a contrast of $\sim 88\%$. Scale bar in (c) and (d): 200 nm .

4.2. Simulation of the expanded OTF

Figure 4 compares the OTFs of the spinning-disk 3D SIM (Fig. 4(a)) and the wide-field microscopy (Fig. 4(b)). Spinning-disk 3D SIM expands its OTF to 17 distinct directions using the lattice illumination (Fig. 3(b)). As the disk spins, the OTF of the spinning-disk 3D SIM becomes symmetric along the k_z axis. To demonstrate the OTF intensity, Fig. 4 shows the cross-sections of the simulated OTFs along the $k_y - k_z$ plane when $k_x = 0$. The spinning-disk 3D SIM demonstrates a two-fold OTF expansion in all directions and filling of the missing cone. Therefore, this method achieves both resolution doubling and optical sectioning. Because the OTF of the spinning-disk 3D SIM has relatively low intensities in the high-frequency region, the detected images are Wiener filtered [16] to enhance the details and the contrast.

4.3. Images of the fluorescent beads

Figure 5 compares the resolution of wide-field microscopy and the spinning-disk 3D SIM using fluorescent beads (Thermo Fisher Scientific, F8803, diameter 100 nm). A solution of the beads was drop-casted on the coverslip. In the lateral direction, the spinning-disk 3D SIM (Fig. 5(a)) resolves beads that appear as indistinguishable clusters in the wide-field microscopy (Fig. 5(b)). In the axial direction, the spinning-disk 3D SIM (Fig. 5(c)) images the beads with a smaller size than that seen by the wide-field microscopy (Fig. 5(d)). The resolution of the spinning-disk 3D SIM is determined by fitting the intensity distribution of beads using a 3D Gaussian function. The fitted full width at half maximum of the beads is reduced from $261 \text{ nm} \pm 11 \text{ nm}$ to $129 \text{ nm} \pm 3 \text{ nm}$ in the lateral direction, and from $771 \text{ nm} \pm 47 \text{ nm}$ to $388 \text{ nm} \pm 13 \text{ nm}$ in the axial direction.

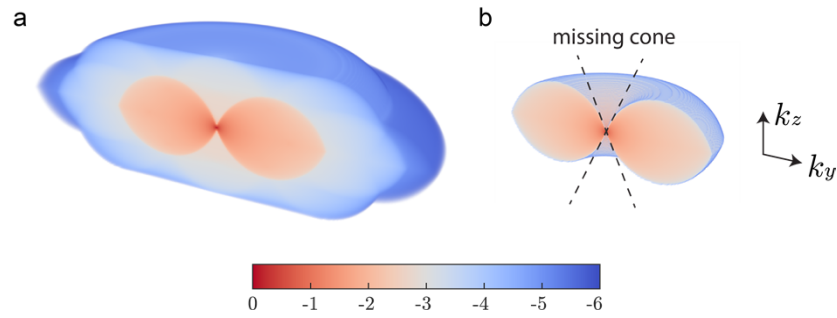


Fig. 4. Comparison of the OTFs of spinning-disk 3D SIM (a) and wide-field microscopy (b). Their intensities are plotted using a logarithmic scale. The spinning-disk 3D SIM expands the wide-field OTF by 2 times in all directions and fills the mission cone.

A further validation of the resolution improvement using image decorrelation analysis [17] can be found in Figure S2. The experimental OTFs are provided in Figure S3.

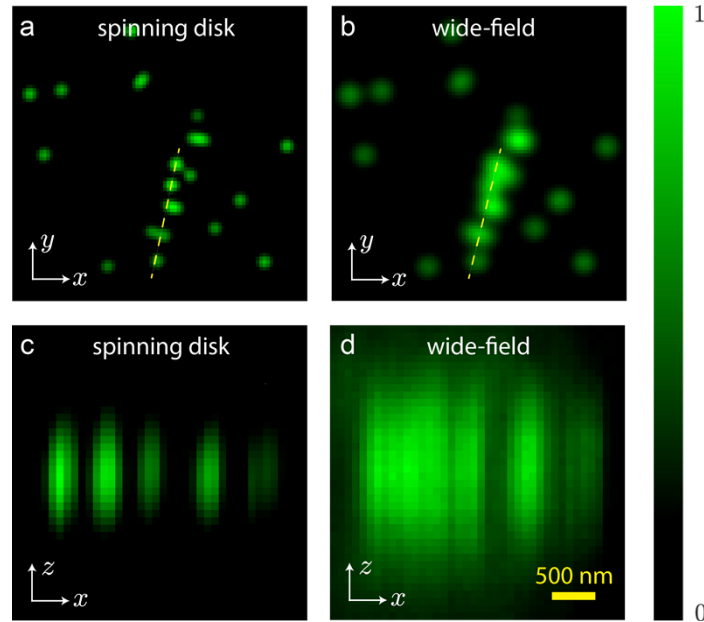


Fig. 5. Images of fluorescent beads obtained using spinning-disk 3D SIM (a and c, wiener filtered) and wide-field microscopy (b and d, raw data). All four images share the same scale bar and have their intensities normalized to one.

4.4. Images of a rat cardiac cell

To illustrate the optical sectioning capability of this method, we imaged the ryanodine receptors in a rat cardiac myocyte with a thickness of around 12 μm . A typical rat cardiac myocyte has a thickness in the range of 10-20 μm , resulting in a strong out-of-focus background in wide-field microscopy (Fig. 6(a) and 6(b)). In conventional 3D SIM, such strong background can obscure the illumination modulation and overwhelm the high-frequency signals, decreasing the spatial resolution [6,7]. In contrast, the spinning-disk 3D SIM produces an image with a much lower background (Fig. 6(c) and 6(d)) by physically rejecting 90% of the out-of-focus signal.

Figure 6(c) and 6(d) show the axial cross-sections along the dashed lines in Fig. 6(a) and 6(b), respectively. The improved resolution and lowered background allow the spinning-disk 3D SIM to identify nearby clusters of the ryanodine receptors that are indistinguishable in conventional microscopy. Figure 6(e) shows the zoom-in areas labelled in Fig. 6(a-d). Significantly more details are visible with the spinning-disk 3D SIM. A video showing 3D cell images is given in the Supplementary Material ([Visualization 1](#)). The doubling of the spatial resolution is validated by image decorrelation analysis (Figure S4).

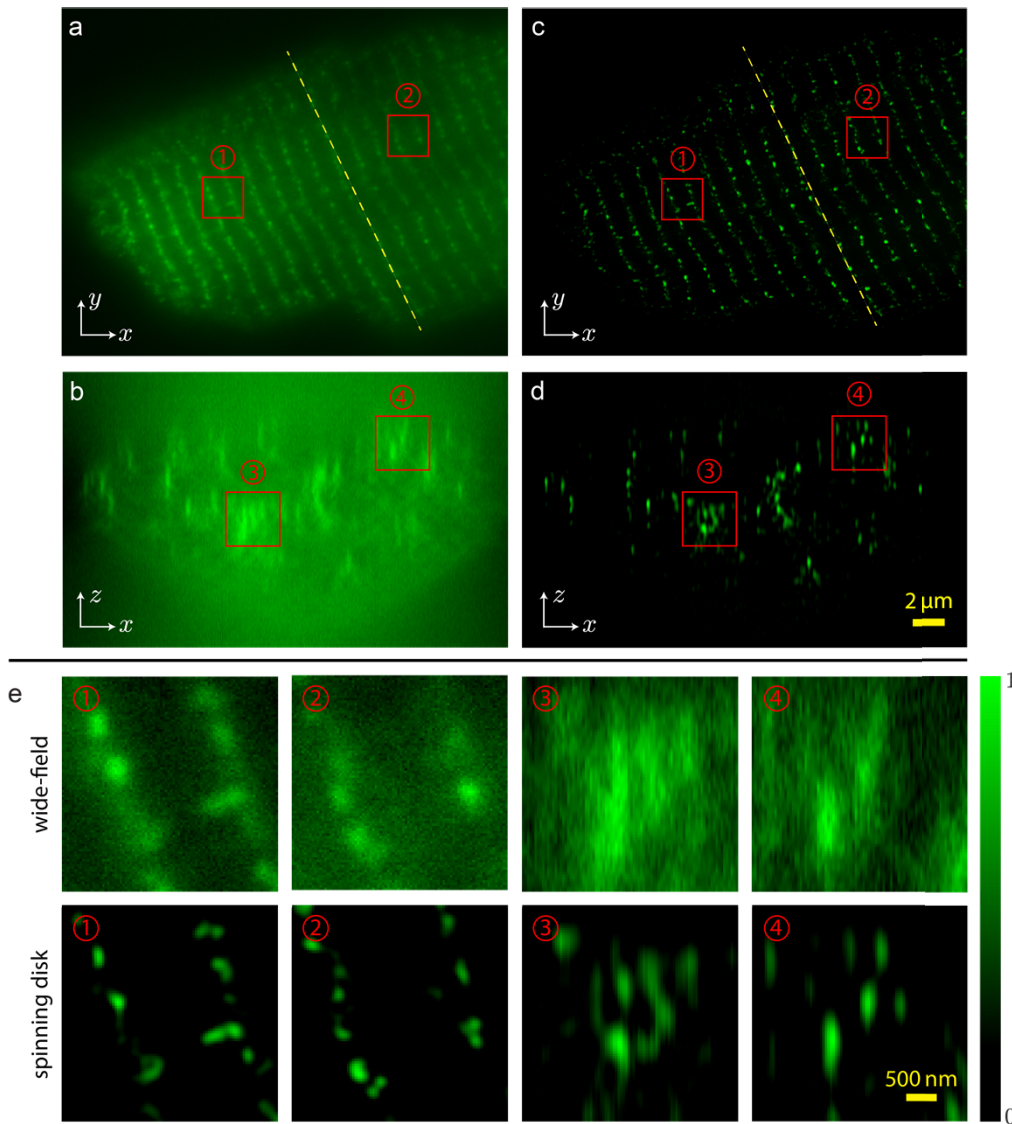


Fig. 6. Fluorescence images of ryanodine receptors in a rat cardiac myocyte at the depth of 6 μm . The cell has a total thickness of around 12 μm . (a-b) Wide-field images of the sample. (c-d) Spinning-disk 3D SIM images of the sample. The axial slices in (b) and (d) are cross sections along the yellow dashed line in (a) and (c), respectively. Figure (a-d) shares the same scale bar. (e) Zoom-in areas shown by the red boxes in Figure (a-d).

5. Conclusions

This study presents a novel approach for 3D SIM using a spinning disk. The spinning-disk 3D SIM addresses limitations associated with conventional 3D SIM, such as slow imaging speed and vulnerability to out-of-focus background. The disk generates 3D lattice illumination on the sample and optically reconstructs the super-resolved images in real-time. This technique achieves a high imaging speed up to 100 Hz while physically rejects 90% of the background. The performance of this approach is demonstrated by imaging fluorescent beads and the ryanodine receptors in a rat cardiac myocyte with a thickness of around 12 μm .

Funding. Canadian Institutes of Health Research (148527); Canada Foundation for Innovation; Natural Sciences and Engineering Research Council of Canada (2019-05509).

Disclosures. The authors declare no conflicts of interest.

Data availability. The computer codes that support the findings of this study are available at [18]. Data available upon request.

Supplemental document. See [Supplement 1](#) for supporting content.

References

1. R. Heintzmann and C. G. Cremer, "Laterally modulated excitation microscopy: improvement of resolution by using a diffraction grating," in *Optical Biopsies and Microscopic Techniques III, Proceedings of the BiOS Europe '98*, I. J. Bigio, H. Schneckenburger, and J. Slavik, *et al.*, eds. (SPIE Press, 1999), pp. 185–196.
2. T. A. Klar and S. W. Hell, "Subdiffraction resolution in far-field fluorescence microscopy," *Opt. Lett.* **24**(14), 954 (1999).
3. M. G. L. Gustafsson, D. A. Agard, and J. W. Sedat, "Doubling the lateral resolution of wide-field fluorescence microscopy using structured illumination," in *Three-Dimensional and Multidimensional Microscopy: Image Acquisition Processing VII, Proceedings of the BiOS 2000 The International Symposium on Biomedical Optics*, J.-A. Conchello, C. J. Cogswell, and A. G. Tescher, *et al.*, eds. (SPIE Press, 2000), pp. 141–150.
4. E. Betzig, G. H. Patterson, and R. Sougrat, *et al.*, "Imaging intracellular fluorescent proteins at nanometer resolution," *Science* **313**(5793), 1642–1645 (2006).
5. M. J. Rust, M. Bates, and X. Zhuang, "Sub-diffraction-limit imaging by stochastic optical reconstruction microscopy (STORM)," *Nat. Methods* **3**(10), 793–796 (2006).
6. M. G. L. Gustafsson, L. Shao, and P. M. Carlton, *et al.*, "Three-dimensional resolution doubling in wide-field fluorescence microscopy by structured illumination," *Biophys. J.* **94**(12), 4957–4970 (2008).
7. L. Gao, L. Shao, and C. D. Higgins, *et al.*, "Noninvasive imaging beyond the diffraction limit of 3D dynamics in thickly fluorescent specimens," *Cell* **151**(6), 1370–1385 (2012).
8. S. Hayashi and Y. Okada, "Ultrafast superresolution fluorescence imaging with spinning disk confocal microscope optics," *Mol. Biol. Cell* **26**(9), 1743–1751 (2015).
9. M. G. L. Gustafsson, D. A. Agard, and J. W. Sedat, "Sevenfold improvement of axial resolution in 3D wide-field microscopy using two objective lenses," in *Three-Dimensional Microscopy: Image Acquisition and Processing II, Proceedings of the IS&T/SPIE's Symposium on Electronic Imaging: Science & Technology*, T. Wilson and C. J. Cogswell, eds. (SPIE Press, 1995), pp. 147–156.
10. H.-C. Huang, B.-J. Chang, and L.-J. Chou, *et al.*, "Three-beam interference with circular polarization for structured illumination microscopy," *Opt. Express* **21**(20), 23963 (2013).
11. M. Petráň, M. Hadravský, and M. D. Egger, *et al.*, "Tandem-scanning reflected-light microscope," *J. Opt. Soc. Am.* **58**(5), 661 (1968).
12. P. Asghari, M. Schulson, and D. R. L. Scriven, *et al.*, "Axial tubules of rat ventricular myocytes form multiple junctions with the sarcoplasmic reticulum," *Biophys. J.* **96**(11), 4651–4660 (2009).
13. M. G. L. Gustafsson, D. A. Agard, and J. W. Sedat, "Sevenfold improvement of axial resolution in 3D wide-field microscopy using two objective lenses," in T. Wilson and C. J. Cogswell, eds. *Three-Dimensional Microscopy: Image Acquisition and Processing II* (1995), pp. 147–156.
14. B. Richards and E. Wolf, "Electromagnetic diffraction in optical systems, II. Structure of the image field in an aplanatic system," *Proc. R. Soc. Lond. A* **253**(1274), 358–379 (1959).
15. Q. Li, "Optimization of point spread function of a high numerical aperture objective lens : application to high resolution optical imaging and fabrication," Ph.D. Thesis, École normale supérieure de Cachan - ENS Cachan (2014).
16. D. A. Agard, Y. Hiraoka, and P. Shaw, *et al.*, "Fluorescence microscopy in three dimensions," *Methods Cell Biol.* **30**, 353–377 (1989).
17. A. Descloux, K. S. Grunmayer, and A. Radenovic, "Parameter-free image resolution estimation based on decorrelation analysis," *Nat. Methods* **16**(9), 918–924 (2019).
18. Y. Zhang, P. Asghari, and D. R. L. Scriven, *et al.*, "3D structured illumination microscope using a spinning disk: code," Github, 2019, <https://github.com/youchang-z/SD-3DSIM>